Supplementary information: Influence of radial transport and turbulent effects on CO₂ conversion in a microwave plasma reactor: Insights from a thermo-chemical flow model.

Helder M.S. Van Poyer, Ivan Tsonev, Stein J.R. Maerivoet, Matthias Albrechts, Annemie Bogaerts

Research Group PLASMANT, Department of Chemistry, University of Antwerp, Universiteitsplein 1, BE-2610 Wilrijk-Antwerp, Belgium

S.1. Plasma size measurements as a function of input power

The plasma size is adopted from the experiments at 1 bar and 20 slm and applied in the model for all different flow rates. Both the length and width of the plasma are almost independent of flow rate.
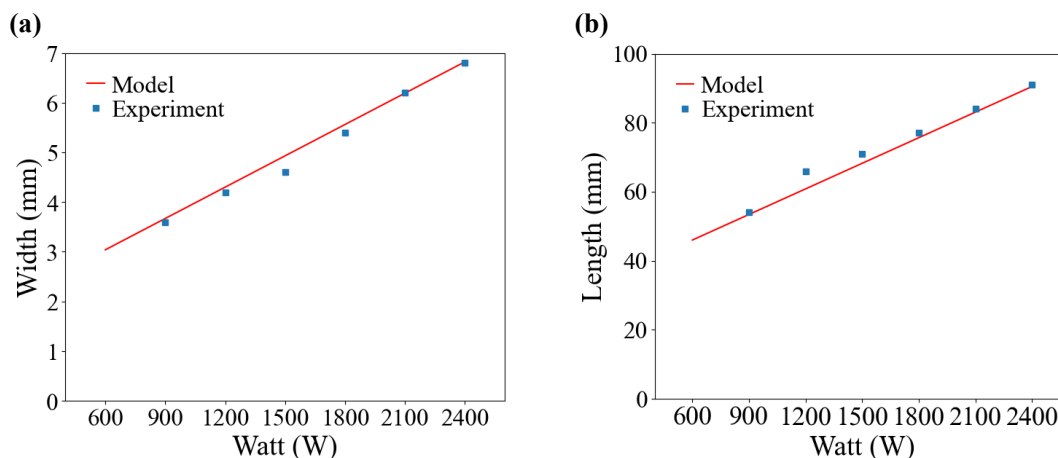

Figure S.1. Plasma width (a) and length (b) as digitized from measured data by D'Isa for 1 bar and 20 slm (blue squares) [1] compared to interpolation used in the model to describe the heat source based on the input power (red).

The values of X and Y of figure 2 in the main paper correspond with the plasma width and length for a given input power presented in Figure S.1. We applied an interpolation function to present the plasma size in each dimension for the given input powers, since the dependence on flow rate is negligible. For the full experimental work, we refer to [1]. Note that an increase in plasma power leads to an increase in the volume of the heat source, and consequently, deposited power and power density are not directly proportional.

S.2.   Meshing of the simulation domain

S.2.1.   3D Mesh

The 3D mesh consists of 17,792,576 mesh elements, of which 15,910,456 are tetrahedral elements, 1,882,120 are prisms, 198,312 are triangles 3400 are quads, 340 are edge elements and 10 are vertex elements. The mesh size is illustrated in Figure S.2.
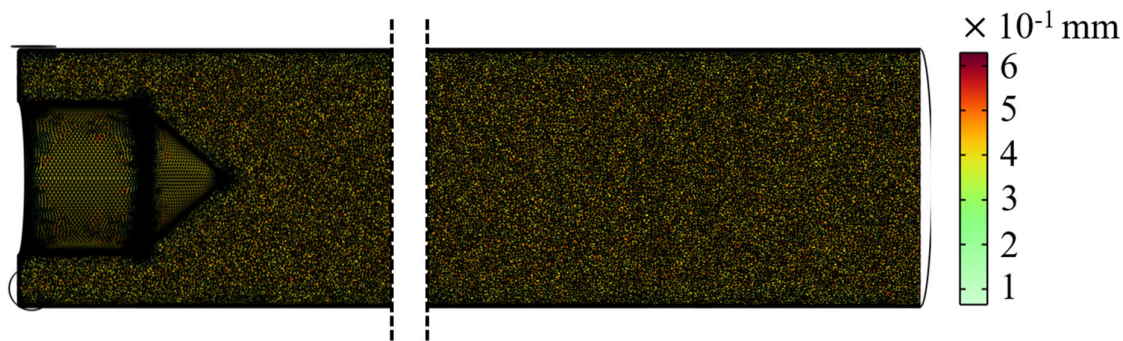

Figure S.2. Mesh plot of the 3D fluid domain, representing the mesh size.

The mesh was refined by reducing the maximum and minimum element size by 50% until negligible (<1%) changes in maximum velocity in the reactor were obtained, and the maximum element size was set to be 0.4 mm and the minimum element size to 0.1 mm.

S.2.2.   2D axi-symmetric mesh

The 2D axisymmetric mesh consists of 1,034,434 mesh elements, of which 983,714 are triangles, 50,720 are quads, 8523 are edge elements and 9 are vertex elements. The mesh size is illustrated in Figure S.3.
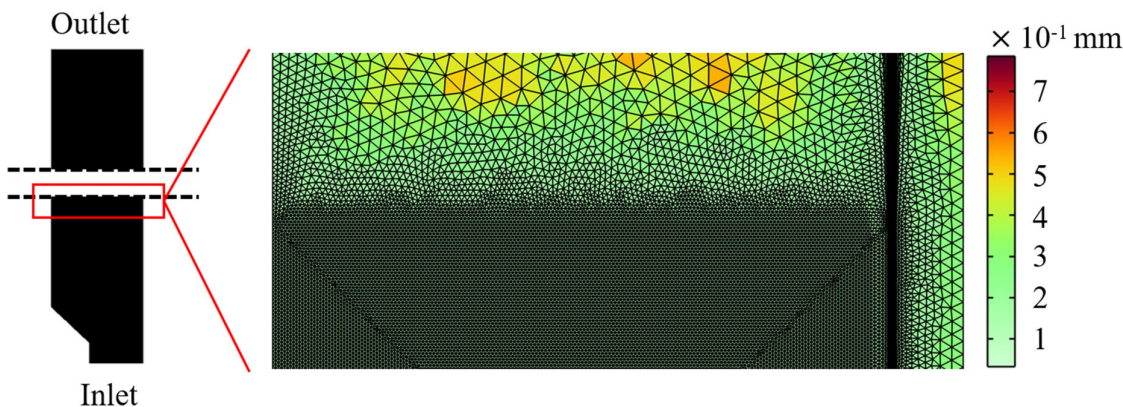

Figure S.3. Mesh plot of the 3D fluid domain, representing the mesh size of the region where the mesh size transitions.

From Figure S.3 it is apparent that the mesh is too dense to plot at once, the inlet region of the mesh was plotted, to show the mesh density. The mesh was first refined by reducing the maximum and minimum element size by 50% until negligible changes (<1%) in global variables (e.g., maximum temperature, maximum velocity magnitude and conversion) were observed. The mesh was further refined until negligible changes in local values (local reaction and transport rates) were observed.

The region from the inlet to an axial position of 16 cm has a finer mesh, with the maximum mesh element size set to 0.0772 mm and the minimum mesh element size set to 2.9×10^{-4} mm. The longest heat source at 2400 W is well below 10 cm as can be seen from Figure S.1 (b). The afterglow region to the outlet is meshed with the maximum element size set to 0.189 mm and the minimum element size

set to 2.18×10^{-3} mm. In the afterglow the temperature gradients are significantly less steep, requiring a less dens mesh.

Finally, in order to validate whether our mesh is fine enough to resolve the boundary layer near the wall, we used the distance to the cell center in viscous units, which is less than 0.5 for all of our simulation results, as suggested for modelling the low-Reynolds formulation of the boundary layers in [2].

S.3.   Thermophysical properties of the quartz tube

Figure S.4 presents the thermal conductivity (left) and the heat capacity (right) of the quartz tube, as a function of temperature.
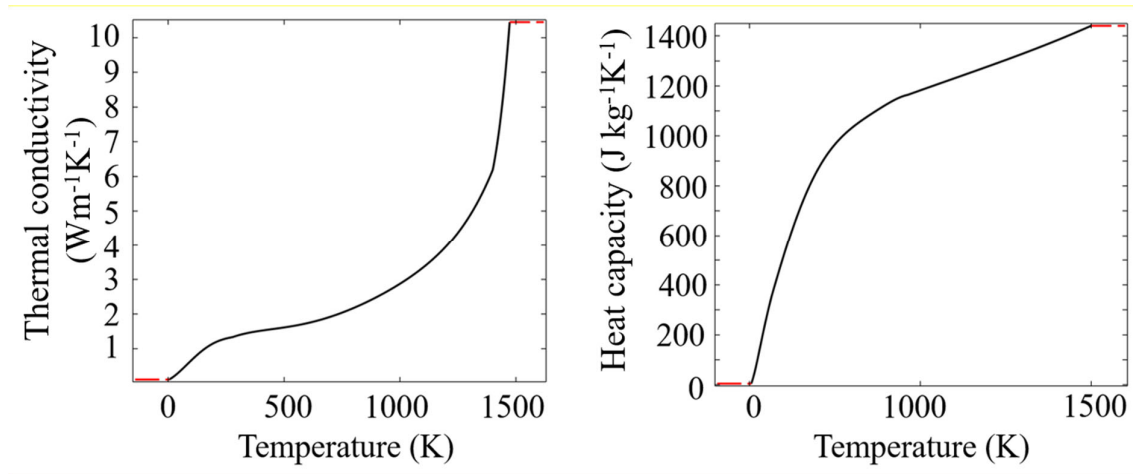

Figure S.4. Thermophysical properties of the quartz tube as a function of temperature: thermal conductivity (left) and heat capacity (right).

Nearly all multi-dimensional CO_2 models from literature do not solve for surface-to-ambient radiation (e.g., [3-6]). In contrast to these models, we considered surface-to-ambient radiation in our model, by employing the Stefan-Boltzmann law at the HA-boundary (see Table 2 of the main paper) in the 2D axisymmetric model. We found that applying the surface-to-ambient radiation at the AH boundary significantly reduces the gas temperature at the edges of the fluid domain (BG). This is due to more efficient heat dissipation through the quartz wall out of the simulation domain compared to only convective heat loss at this boundary, as can be seen in Figure S.5
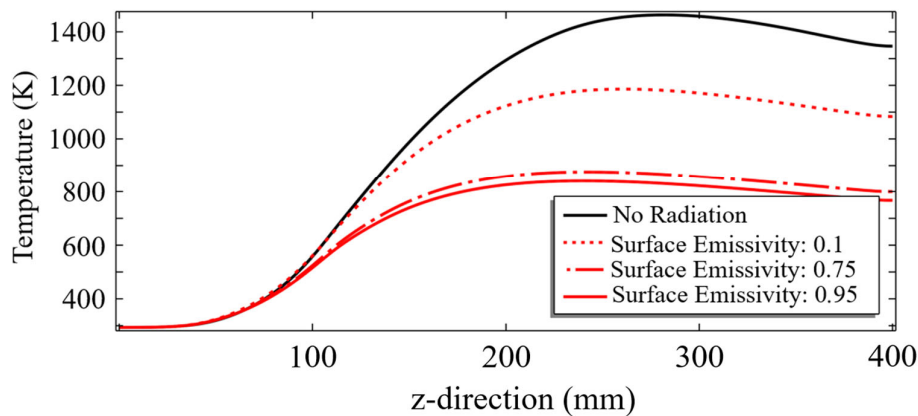

Figure S.5. Axial temperature profile at the HA boundary for different emission coefficients, for 10 slm, 1500 W and 1 atm.

The reported surface emissivity for quartz tubes varies in literature from 0.67-0.95 [7-9]. We applied a surface emissivity of 0.75 in our model. As can be seen from Figure S.5, higher values of this coefficient have a negligible effect on the gas temperature near the quartz wall. The temperature variation between the inner and outer boundary of the quartz tube is never more than 25 K for the conditions under study. Generally, one could take the temperature at the edge of the fluid domain as a proxy for the temperature at the edge of the simulation domain and avoid modelling the quartz tube.

S.4. Turbulent viscosity and SST variables

The turbulent viscosity, μ_T used in Eq.5 in section 2.2 of the main paper is defined as [10]:

$$\mu_T = \frac{a_1 k}{\max{(a_1\omega, Sf_{v2})}} \tag{1}$$

With f_{v2}, a blending function, defined as:

$$f_{v2} = \tanh(\theta_2^2) \tag{2}$$

$$\theta_2 = max\left(\frac{2\sqrt{k}}{\beta_0^*\omega l_w}, \frac{500\,\mu}{\rho\omega l_w^2}\right) \tag{3}$$

With S the measure of the strain rate and l_w the distance closest to the wall. β_0^* is a model constant. The model constants are defined through an interpolation function:

$$\emptyset = f_{v1}\emptyset_1 + (1 - f_{v1})\emptyset_2 \qquad \text{for} \qquad \emptyset = \beta, \gamma, \sigma_k, \sigma_\omega \tag{4}$$

Furthermore, the blending function f_{v1} is defined as:

$$f_{v1} = \tanh(\theta_1^4) \tag{5}$$

$$\theta_1 = min\left[max\left(\frac{\sqrt{k}}{\beta_0^*\omega l_w}, \frac{500\,\mu}{\rho\omega l_w^2}\right), \frac{4\rho\sigma_{\omega2}k}{CD_{k\omega}l_w^2}\right] \tag{6}$$

$$CD_{k\omega} = \max\left(\frac{2\rho\sigma_{\omega2}}{\omega}\nabla\omega \cdot \nabla k, 10^{-10}\right) \tag{7}$$

The constants for the model used in equation 1-7 are $\beta^* = 0.09$, $a_1 = 5/9$, $\beta_1 = 3/40$, $\sigma_{\omega l} = 0.85$, $\sigma_{\omega l} = 0.5$, $a_2 = 0.44$, $\beta_2 = 0.0828$, $\sigma_{k2} = 1$ and $\sigma_{\omega2} = 0.856$, taken from Menter et al. [11]. For further information on the SST model, we refer to [2, 10].

S.5 NASA polynomials for the different species

The thermophysical properties for each species are determined using the nine-term NASA Glenn polynomials which are valid up to 20 000 K [12]. The equations for the polynomials are as follows:

$$C_p°(T) = R\left(a_1 T^{-2} + \frac{a_2}{T} + a_3 + a_4 T + a_5 T^2 + a_6 T^3 + a_7 T^4\right) \tag{8}$$

$$H°(T) = RT\left(-a_1 T^{-2} + a_2\frac{\ln T}{T} + a_3 + a_4\frac{T}{2} + a_5\frac{T^2}{3} + a_6\frac{T^3}{4} + a_7\frac{T^4}{5} + \frac{b_1}{T}\right) \tag{9}$$

$$S°(T) = R\left(-a_1\frac{T^{-2}}{2} - \frac{a_2}{T} + a_3\ln T + a_4 T + a_5\frac{T^2}{2} + a_6\frac{T^3}{3} + a_7\frac{T^4}{4} + b_2\right) \tag{10}$$

With $C_p°(T)$ the molar heat capacity at constant pressure, at temperature T, $H°(T)$ the molar enthalpy at temperature T relative to the molar enthalpy at 0 K, and $S°(T)$ the entropy at temperature T, all for standard state. The standard state, denoted with °, refers to the standard state of the ideal gas at 1 atm.

S.6. Calculation of the thermal conductivity and dynamic viscosity of species i:

Equation 11 represents the calculation of the thermal conductivity of species i [13]:

$$k_{m,i} = 2.669 \times 10^{-6} \frac{\sqrt{TM_i \times 10^3}}{\sigma_i^2 \Omega_k} \times \frac{1.15 C_{p,i} + 0.88 R_g}{M_i} \tag{11}$$

$$\Omega_k = \frac{b_1}{(T^*)^{b_2}} + \frac{b_3}{exp(b_4 T^*)} + \frac{b_5}{exp(b_6 T^*)} + \frac{4.998 \cdot 10^{-40} \mu_{D,i}^4}{k_b^2 T^* \sigma_i^6}, \quad T^* = T\frac{\varepsilon_i}{k_b} \tag{12}$$

With the characteristic length of the Lennard-Jones potential represented by σ_i and the dimensionless collision integral indicated by Ω_k. $C_{p,i}$ the heat capacity at constant pressure of the individual species, M_i the molar mass of the individual species and R_g is the ideal gas constant. In equation 12, b_x are empirical constants, $\mu_{D,i}$ is the dipole constant of species i (D), ε_i is the potential energy minimum value (J) and k_b is Boltzmann's constant (J K^{-1}). Finally, μ and ρ also depend on the chemical composition. The former is calculated using:

$$\mu = \sum_{i=1}^{n} \frac{\mu_i}{1 + \frac{1}{x_i}\sum_{j=1, j\neq i}^{n} x_j \phi_{ij}}, \quad \phi_{ij} = \frac{(1 + (\mu_i/\mu_j)^{0.5}(M_j/M_i)^{0.25})^2}{(4/\sqrt{2})(1 + M_i/M_j)^{0.5}} \tag{13}$$

$$\mu_i = 2.669 \times 10^{-6} \frac{\sqrt{TM_i \times 10^3}}{\sigma_i^2 \Omega_D} \tag{14}$$

$$\Omega_D = \frac{b_1}{(T^*)^{b_2}} + \frac{b_3}{exp(b_4 T^*)} + \frac{b_5}{exp(b_6 T^*)} + \frac{4.998 \times 10^{-40} \mu_{D,i}^4}{k_b^2 T^* \sigma_i^6}, \quad T^* = T\frac{k_b}{\varepsilon_i} \tag{15}$$

With x_i is the molar fraction, μ_i the dynamic viscosity of species i, Ω_D the dimensionless collision integral and ρ the density [13].

S.7. Full experimental dataset compared to the modelled range.

As discussed in section 3.1 of the main paper, our model is not yet able to reproduce the CO_2 conversion in the full experimental range of SEI values. Figure S.6 presents the full SEI range, as provided by D'Isa et al. [1].
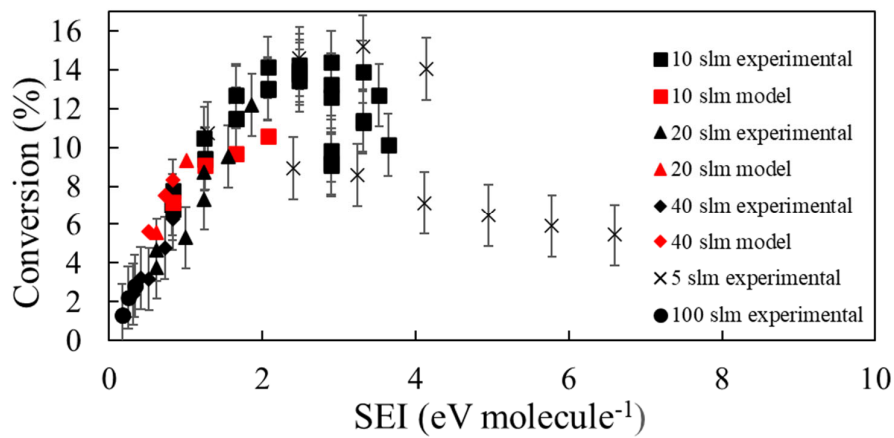

Figure S.6 Full experimental dataset as presented by D'Isa et al. [10], compared with the conditions modelled in the main paper.

Our model was not validated for 100 slm flow rate, since the observed conversion is in the order of magnitude of the error bars, and furthermore, no temperature measurements were provided for this flow rate. As discussed in section 3.1 of the main paper, higher SEI measurements could not yet be reproduced by our model, due to reactions persisting until the end of the simulation domain.

S.8. Sensitivity analysis heat source expanded

It was reported by Viegas et al. that optical contraction can happen in CO_2 plasmas below 150 mbar. The effect is not reported at higher pressures, and Vialetto et al. showed that at 250 mbar, the normalized electron number density and emission intensity profile overlap; nevertheless possible optical contraction is considered here [14]. Viegas et al. suggested a scaling factor of 1.6 when assessing the size of the plasma, that is, the measured width should be multiplied by 1.6 to get the actual plasma width. In our model, the plasma is approximated as a heat source, and therefore, the heat source width is multiplied by 1.5 for identical input power of 1500W at 10 slm and 40 slm. The corresponding power deposition profiles are plotted in Figure S.7.
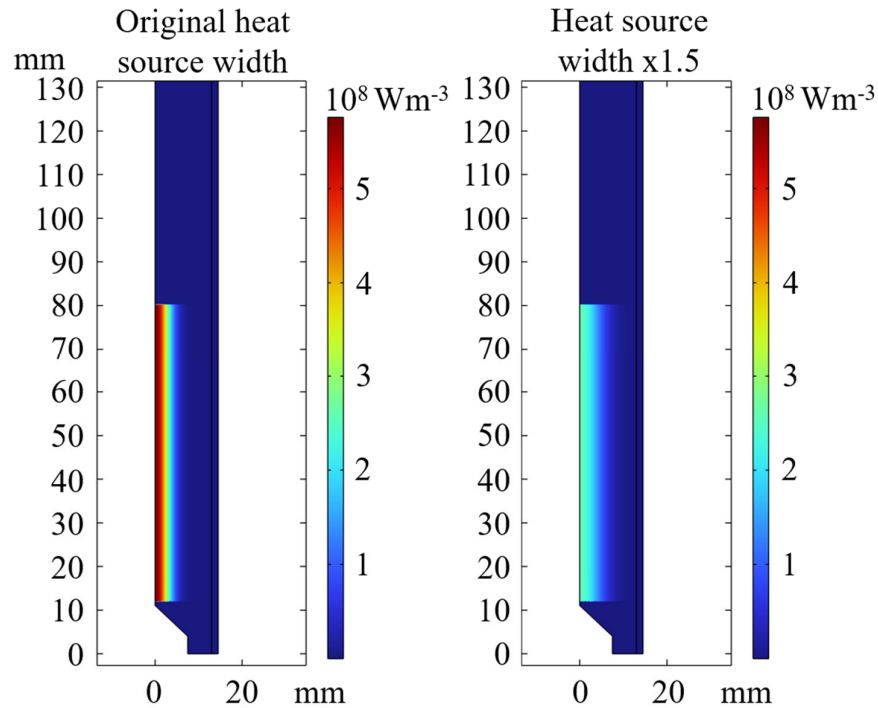

Figure S.7. Heat source profile according to measured data (left) and radially expanded by a factor 1.5 (right)

As can be seen from figure S.8 expanding the power deposition profile by a factor 1.5 actually increases

correspondence with the experiment, as the core temperature drops, which reduces our overestimation of the temperature. The conversion decreases from 10.6% to 10.4% and is thus clearly less sensitive to this change.
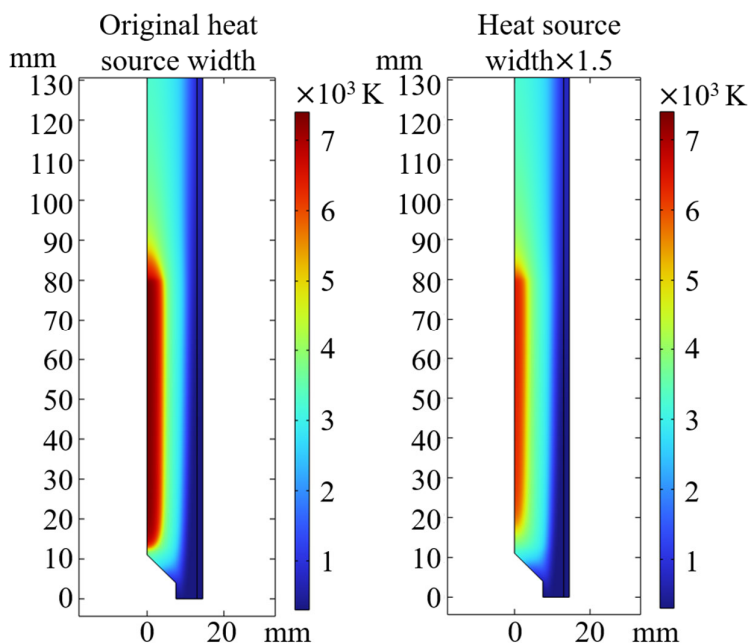
Figure S.8. Temperature profile for original heat source (left) and radially expanded heat source (right) for 10 slm and 1500 W.

However, expanding the heat source at higher flow rates actually results in the gas not being heated efficiently. It should be noted that the temperature scale in Figure S.9 (right) was adapted for clarity.
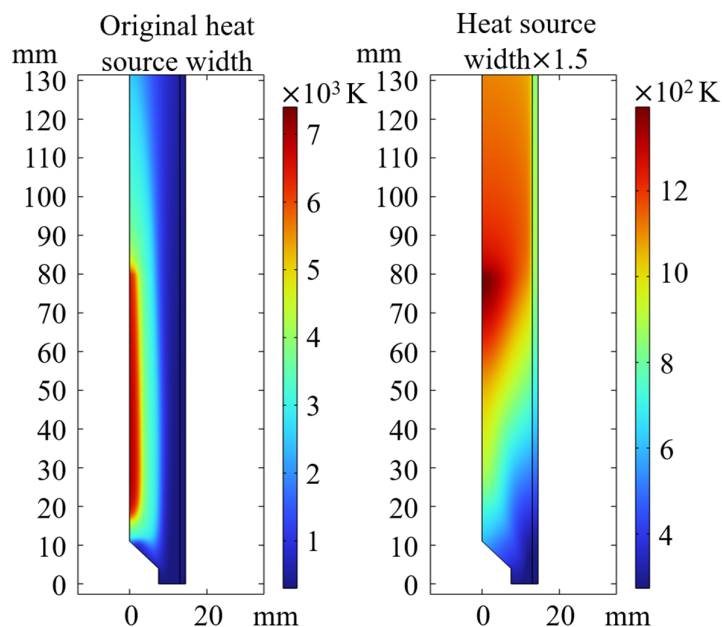

Figure S.9. Temperature profile for original heat source (left) and radially expanded heat source (right) for 40 slm and 1500 W.

Clearly, at 40 slm, drastic changes in the heat source have a significant effect on both temperature profile and conversion, since the temperature does not increase sufficiently enough to dissociate CO_2 at 40 slm, 1500 W for the broader heat source. Therefore, we can conclude that even though fitting the heat source might lead to better agreement with experiment in some conditions, we adhere to the measured plasma dimensions, assuming optical contraction is irrelevant at higher pressure.

S.9 Sensitivity analysis for the initial turbulent intensity

It is known from literature that Menter's SST models are sensitive to the boundary conditions for the specific dissipation rate (ω) [11]. Our models fully resolve the boundary layer using a low-Reynolds formulation at the wall, which is consistent with the no-slip condition. This is checked based on the distance to the cell center in viscous units, as suggested in [2]. The outlet boundary condition is sufficiently far away from the heat source in the model and is therefore assumed to have limited effect.

Lastly, at the inlet both k and ω need to be specified. These results might affect the results further in the domain. Both k and ω can be averaged over the φ-direction analogous to the velocity (see section 2.1 of the main paper), and the results over the inlet for 40 slm are plotted in figure S.10.
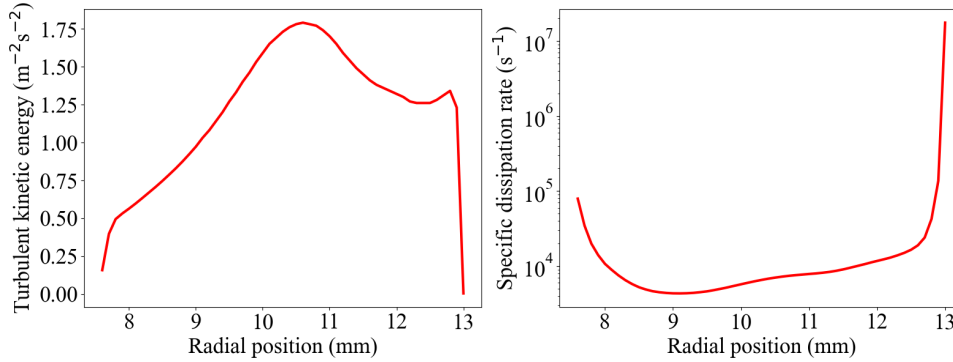

Figure S.10. Turbulent kinetic energy (left) and specific dissipation rate (right) for 40 slm at the inlet of the 2D domain, derived by averaging over the phi-direction in the 3D model.

Alternatively, a value for k (0.005 m^2 s^{-2}) and ω (20 s^{-1}) can be chosen at the inlet, as is done in the main paper. This means that both the turbulent kinetic energy and the turbulent dissipation rate vary over two orders of magnitude at the inlet. We compare both methods at the highest flow rate, which corresponds to the strongest turbulence. Figure S.11 shows the relative turbulent intensity for the chosen values (left) and the interpolated values from the 3D model (right).
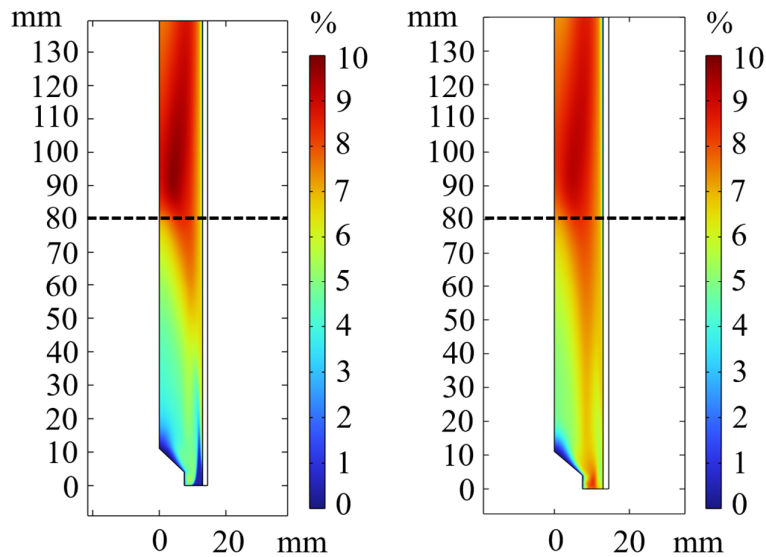

Figure S.11 Comparison of relative turbulent intensity for fixed values of k and ω (left) and for the interpolated values (right) for 40 slm and 1500 W.

As can be seen in Figure S.11, the turbulent intensity profiles are somewhat different for both cases. This results in variations in the core plasma temperature, however, as discussed in the main paper (section 3.2) and in the SI section S.8, significant deviations in the temperature profile are required to really affect the conversion. Moreover, as discussed in section 3.7.3 of the main paper, turbulence needs to be significantly enhanced to promote conversion, as indicated by Table 3 of the main paper. The temperature profile is plotted for 40 slm and 1500 W in Figure S.12.
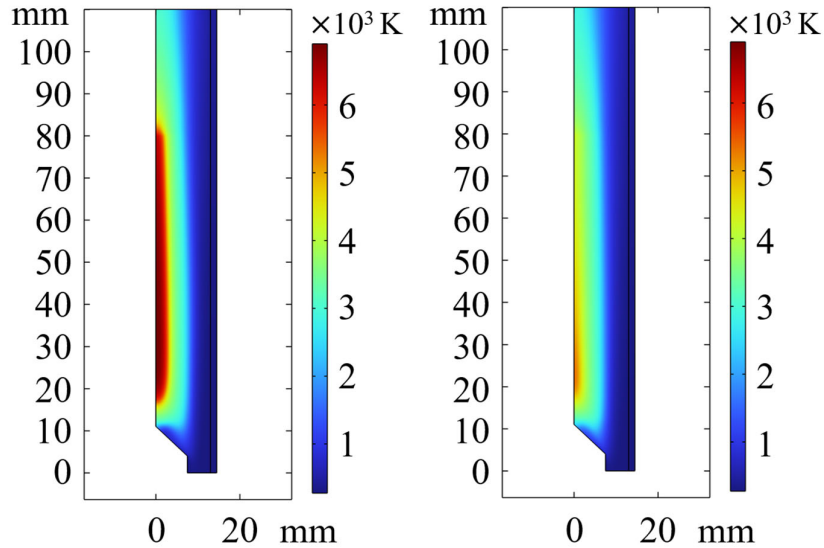

Figure S.12 Comparison of temperature profile for fixed values of k and ω (left) and for the interpolated values (right) for 40 slm and 1500 W.

As can be seen in the figure, there is a strong drop in core plasma temperature when the interpolated values for k and ω are employed (right). Nevertheless, as discussed in section 3.2 of the main paper, the conversion shows only limited sensitivity with respect to the temperature profile. Moreover, as discussed in section 3.5 of the main paper, all C atoms are created by dissociation of CO, and diffusion of C atoms can only cause additional conversion upon reacting with CO_2 according to R5, which does not occur. The core plasma temperature, which determines the dissociation rate of CO, is thus of lesser importance, as shown in section 3.2 of the main paper. Moreover, at lower flow rates, as well as at higher SEI, the effects become significantly less pronounced, as plotted in Figure S.13.
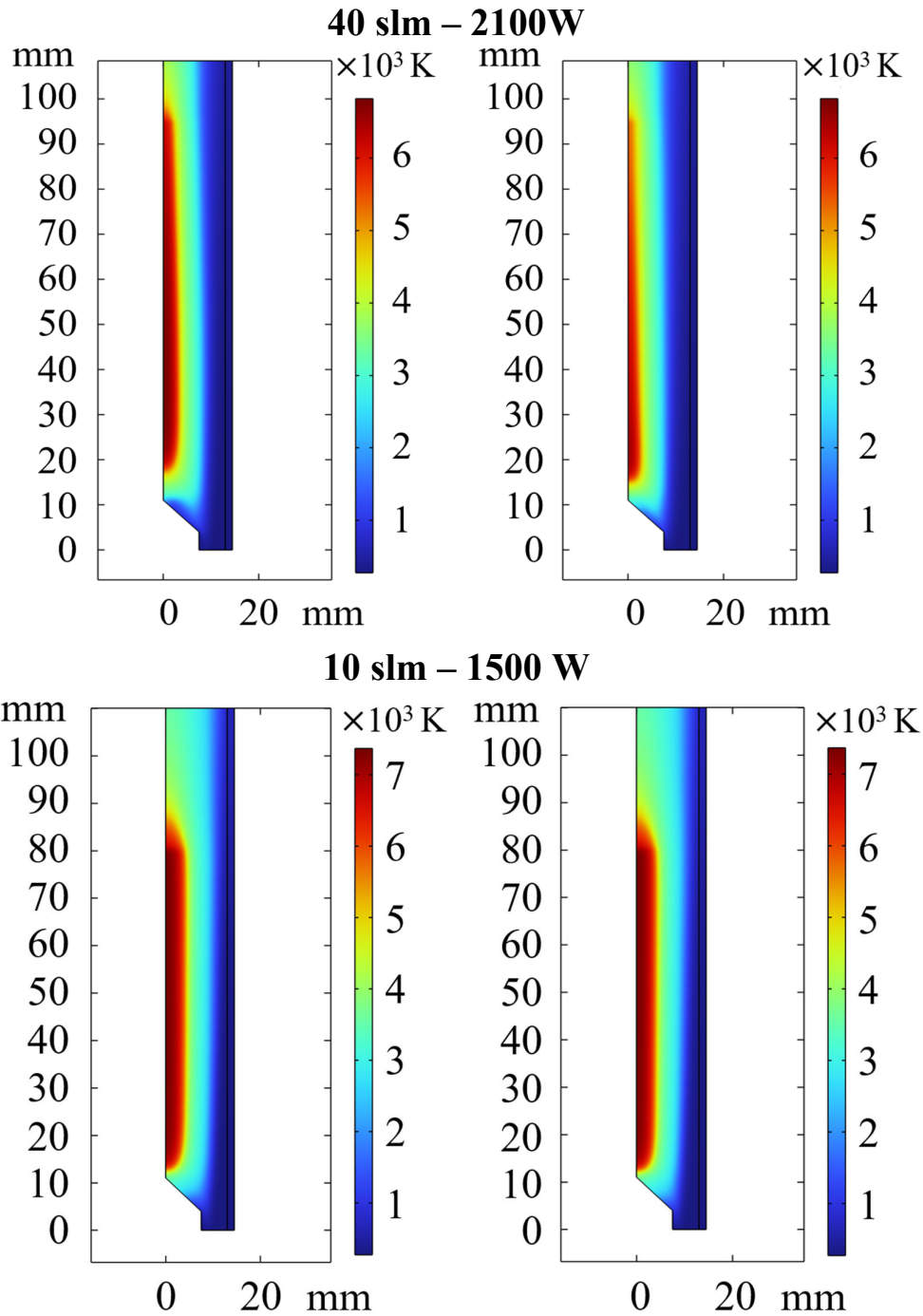
Figure S.13. Comparison of temperature profile for fixed values of k and ω (left) and for the interpolated values (right), for 40 slm and 2100 W (top) and for 10 slm and 1500 W (bottom).

As can be seen in Figure S.13, when increasing the SEI at the highest flow rate (40 slm), the differences in temperature profile become less pronounced, whereas at the highest SEI condition and the lowest flow rate (10 slm), the differences are completely negligible.

All conclusions in the main paper are thus valid for both values of the turbulent kinetic energy and the specific dissipation rate at the inlet. The fixed values for turbulent kinetic energy and specific dissipation rate are used in the main paper, since computationally, they converge to a solution more easily.

S.10 There is no chemical equilibrium and LTE in CO_2 MW plasma: Need for coupling all physics within the model

In LTE, the plasma's local composition depends solely on temperature and pressure [15, 16]. To evaluate the validity of the LTE approximation, we disregarded transport of species in our model, for the same gas flow velocity and temperature profiles, and hence, the temperature and pressure are kept identical. Diffusion is neglected by reducing all diffusion coefficients (cf. equation 12) to 1% of their original value, while turbulent diffusion is neglected by setting the turbulent Schmidt number (cf. equation 18) to 10^6 (the turbulent Schmidt number of a single species does not exceed 1.7 in any of the modelled conditions), and finally convective transport of species is ignored by setting the gas velocity in equation 8 to zero.

Figure S.14 shows the calculated mole fractions of the various species, when solving the thermo-chemical model (solid) and when neglecting transport (dashed), on a radial cutline taken at an axial position of 55 mm (i.e., the plasma center), for 1200 W, 10 slm and 1 atm. Note that the exact axial position for analyzing the molar fractions is not important, as long as it is within the plasma core, since the gradients in the z-direction are negligible, at least when we assume a rectangular function for the heat source along the axial direction. However, the gradients in the z-direction become important in the afterglow region.
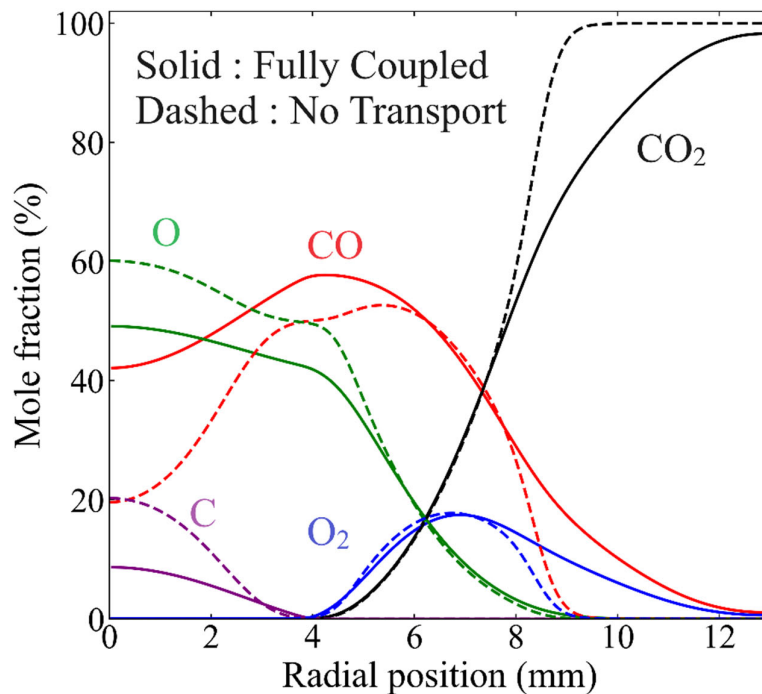

Figure S.14. Comparison of calculated molar fractions of the various plasma species along a radial cut line at z = 55 mm, for 1200 W, 10 slm and 1 atm, for a solution where all physics considered in the model are fully coupled of the model (solid) and when transport of species is neglected (dashed).

As discussed above, within the LTE approximation, the local plasma composition does not depend on the transport of species. However, Figure S.14 shows that when transport of species is neglected, the molar concentration profiles differ strongly from the solution where all physics considered in the model are fully coupled. Consequently, LTE is not obtained, due to deviations in chemical equilibrium.

Indeed, to achieve chemical equilibrium in a CO_2 plasma, transport (predominantly diffusion) processes must be significantly slower than the reaction kinetics. When the total rate of all forward reactions in

which a species participates, is identical to the total rate of all backward reactions, chemical equilibrium is obtained. However, if the formed species is transported away before the backward reaction can take place, no chemical equilibrium is obtained. Hence, the difference between the solid and dashed lines in Figure S.14, i.e., with and without transport of species, clearly demonstrates that transport is important, and fast enough to disrupt chemical equilibrium.

Diffusion is fast enough to disrupt chemical equilibrium in the MW CO_2 plasma, because the large temperature gradient along the radial direction (cf. 6(a) of the main paper) results in large concentration gradients, promoting diffusion. Only between 6 and 8 mm, the LTE mole fractions correspond roughly with the mole fractions obtained with the solution where all physics considered in the model are fully coupled. However, as will be illustrated in section Figure S.15 below, there is still net production and transport in this region, indicating that also here chemical equilibrium is not obtained. In summary, it is clear that solving the transport of species, which drives the chemical non-equilibrium, is key in accurately assessing the CO_2 conversion. In the next section, we will evaluate the importance of transport by diffusion vs convection.

This discrepancy in mole fractions is sufficient evidence that LTE is not valid, and the influence of transport phenomena on the net rates, that are discussed in section 3.5 and 3.6 of the main paper, might not be as apparent.

Therefore, Figure S.15 shows the different components governing conservation of mass (cf. equation 8 of the main paper) of CO for steady state conditions, when neglecting transport, as a function of radial position, for an axial position of 55 mm (i.e., the plasma center). As transport phenomena are not taken into account, only the net reaction rates are plotted, because the net diffusive and convective flux of CO are zero. This figure should be compared with Figure 9 in the main paper, where transport is taken into account.
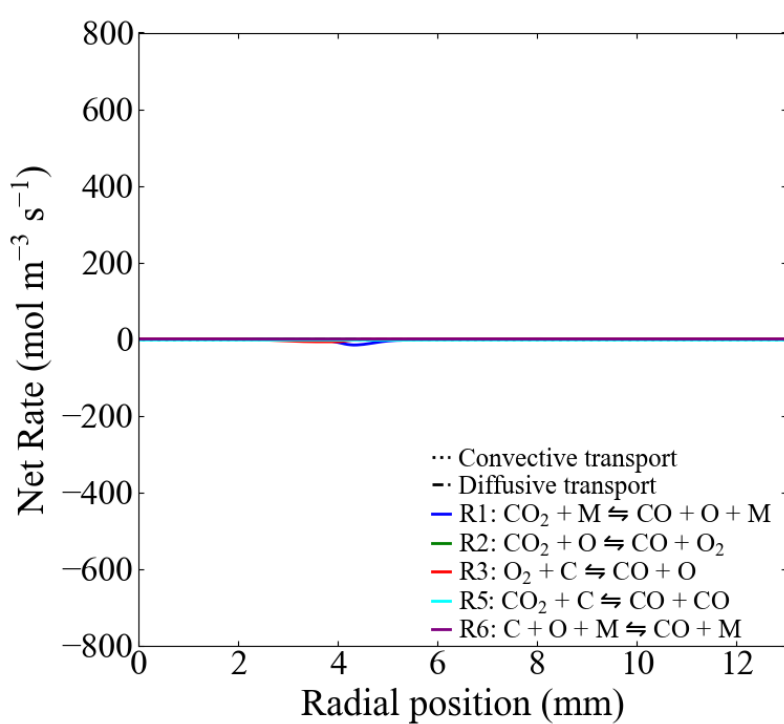

Figure S.15. Calculated net reaction rates of reactions involving CO atoms, neglecting transport, as a function of radial position, at an axial position of 55 mm, for 10 slm, 1200 W and 1 atm. The sign of the reaction rates is chosen so that positive values correspond to net CO production. The scale of the y-axis is kept the same as in Figure 9, for a 1-on-1 comparison.

As is apparent from Figure S.15, chemical equilibrium is reached when transport phenomena are neglected, because the net reaction rates are (close to) zero. There are very small deviations from zero, due to the numerically small diffusion. Moreover, by comparing to Figure 9 in the main paper, it is clear that species transport, mainly diffusion, is important in determining local net production rates.

S. 11 Flow velocity lines and velocity components

Figure S.16 shows the flow lines in 3D across the 2D axisymmetric domain, with the temperature plotted on a cut plane through the center, for 10 slm, 1200 W and 1 atm.
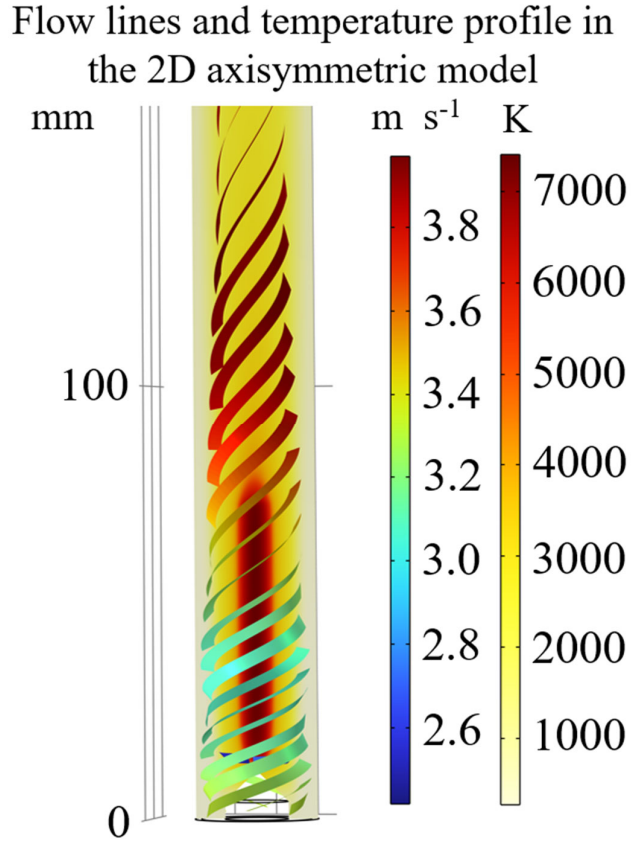

Figure S.16. Flow lines with uniform density and the temperature profile for 10 slm, 1200 W and 1 atm.

The flow lines are spaced with uniform density, and the figure illustrates that the flow speeds up after the plasma and that the swirl is maintained after the plasma. Figure S.17 depicts the different velocity components for 10 slm, 1200 W and 1 atm.
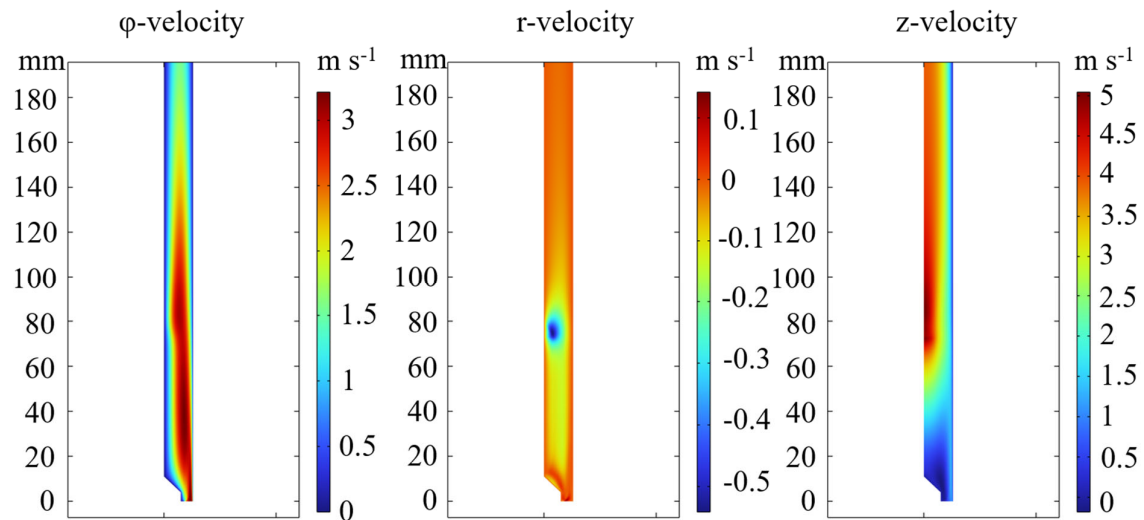
Figure S.17. Velocity components for 10 slm, 1200 W and 1 atm.

As can be seen in Figure S.17, the swirl flow is still present even after the plasma, and the z-velocity in the reactor is almost exclusively positive. Most importantly, the r-velocity is exclusively negative in the reactor, apart from a small region near the inlet. Hence, all convective transport is towards the symmetry axis of the reactor.

S.12 Mole fraction analysis

Figure S.18 shows the difference in CO mole fraction between the laminar and turbulent flow solution, near the reactor outlet. Positive values mean a higher CO mole fraction in the laminar flow solution, while negative values correspond to a lower CO mole fraction.
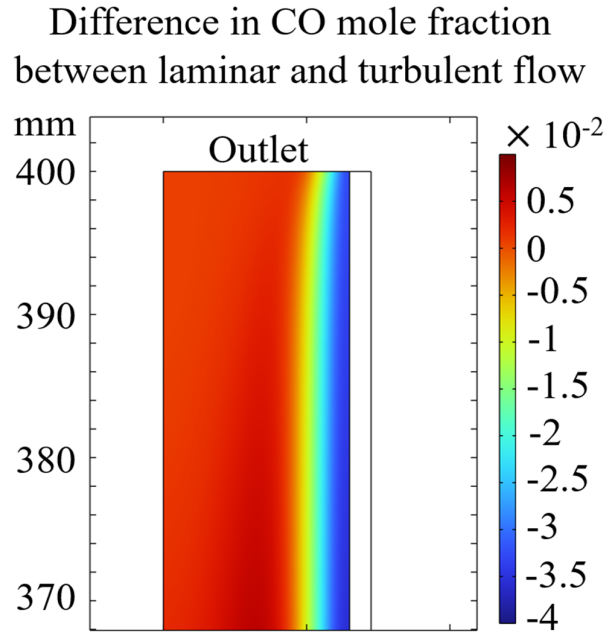

Figure S.18. Difference in mole fraction of CO between the laminar and turbulent solution near the outlet, at 1500 W, 40 slm and 1 atm.

Only at the edge of the fluid domain, there is significantly less CO present in the laminar solution (about 4%), and this result is a direct consequence of turbulent mixing at the edge of the domain. Turbulent diffusion causes more CO to diffuse into the cold gas stream at the edge of the reactor, where it can be transported out by axial convection.

S.13 Bibliography

[1] F. D'Isa, E. Carbone, A. Hecimovic, U. Fantz, Performance analysis of a 2.45 GHz microwave plasma torch for CO2 decomposition in gas swirl configuration, Plasma Sources Science and Technology (2020). https://doi.org/10.1088/1361-6595/abaa84.

[2] COMSOL, Comsol Multiphysics 6.0 CFD Module User's Guide.

[3] S. Van Alphen, A. Hecimovic, C.K. Kiefer, U. Fantz, R. Snyders, A. Bogaerts, Modelling post-plasma quenching nozzles for improving the performance of CO2 microwave plasmas, Chemical Engineering Journal 462 (2023) 142217. https://doi.org/https://doi.org/10.1016/j.cej.2023.142217.

[4] K. Wang, S. Ceulemans, H. Zhang, I. Tsonev, Y. Zhang, Y. Long, M. Fang, X. Li, J. Yan, A. Bogaerts, Inhibiting recombination to improve the performance of plasma-based CO2 conversion, Chemical Engineering Journal 481 (2024) 148684. https://doi.org/https://doi.org/10.1016/j.cej.2024.148684.

[5] V. Kotov, C.K. Kiefer, A. Hecimovic, Validation of the thermo-chemical approach to modelling of the CO2 conversion in sub-atmospheric pressure microwave gas discharges, Plasma Sources Science and Technology (2024).

[6] D.C.M. van den Bekerom, J.M.P. Linares, T. Verreycken, E.M. van Veldhuizen, S. Nijdam, G. Berden, W.A. Bongers, M.C.M. van de Sanden, G.J. van Rooij, The importance of thermal dissociation in CO2 microwave discharges investigated by power pulsing and rotational Raman scattering, Plasma Sources Science and Technology 28(5) (2019) 055015. https://doi.org/10.1088/1361-6595/aaf519.

[7] J. Hildebrand, K. Hecht, J. Bliedtner, H. Müller, Laser Beam Polishing of Quartz Glass Surfaces, Physics Procedia 12 (2011) 452-461. https://doi.org/https://doi.org/10.1016/j.phpro.2011.03.056.

[8] A.J. Wolf, F.J.J. Peeters, P.W.C. Groen, W.A. Bongers, M.C.M. van de Sanden, CO2 Conversion in Nonuniform Discharges: Disentangling Dissociation and Recombination Mechanisms, Journal of Physical Chemistry C 124 (2020) 16806-16819.

[9] B. Barnes, W. Forsythe, E. Adams, The total emissivity of various materials at 100–500° C, JOSA 37(10) (1947) 804-807.

[10] F. Menter, M. Kuntz, R.B. Langtry, Ten years of industrial experience with the SST turbulence model, Heat and Mass Transfer 4 (2003).

[11] F. Menter, Zonal Two Equation k-w Turbulence Models For Aerodynamic Flows, 23rd Fluid Dynamics, Plasmadynamics, and Lasers Conference. https://doi.org/10.2514/6.1993-2906.

[12] B.J. Mcbride, M.J. Zehe, S.D. Gordon, NASA Glenn Coefficients for Calculating Thermodynamic Properties of Individual Species, 2002.

[13] P.D. Neufeld, A.R. Janzen, R.A. Aziz, Empirical Equations to Calculate 16 of the Transport Collision Integrals $\Omega(l, s)*$ for the Lennard-Jones (12–6) Potential, The Journal of Chemical Physics 57(3) (1972) 1100-1102. https://doi.org/10.1063/1.1678363.

[14] L. Vialetto, A.W. van de Steeg, P. Viegas, S. Longo, G.J. van Rooij, M.C.M. van de Sanden, J. van Dijk, P. Diomede, Charged particle kinetics and gas heating in CO2 microwave plasma contraction: comparisons of simulations and experiments, Plasma

Sources Science and Technology 31(5) (2022) 055005. https://doi.org/10.1088/1361-6595/ac56c5.

[15] A.B. Murphy, Thermal plasmas in gas mixtures, Journal of Physics D: Applied Physics 34(20) (2001) R151. https://doi.org/10.1088/0022-3727/34/20/201.

[16] M.I. Boulos, P.L. Fauchais, E. Pfender, Fundamental Concepts in Gaseous Electronics, in: M.I. Boulos, P.L. Fauchais, E. Pfender (Eds.), Handbook of Thermal Plasmas, Springer International Publishing, Cham, 2023, pp. 139-180. https://doi.org/10.1007/978-3-030-84936-8_4.